MIT Open Access Articles

15.7% Efficient 10-μm-Thick Crystalline Silicon Solar Cells Using Periodic Nanostructures

15.7% Efficient 10-µm-Thick Crystalline Silicon Solar Cells Using Periodic Nanostructures

Matthew S. Branham, Wei-Chun Hsu, Selcuk Yerci, James Loomis, Svetlana V. Boriskina, Brittany R. Hoard, Sang Eon Han, Gang Chen*

Dr. Matthew S. Branham, Wei-Chun Hsu, Dr. James Loomis, Dr. Svetlana V. Boriskina, Prof. Gang Chen
Department of Mechanical Engineering, Massachusetts Institute of Technology, 77 Massachusetts Ave., Cambridge, MA 02139, USA
E-mail: gchen2@mit.edu

Prof. Selcuk Yerci
Department of Electrical and Electronic Engineering, Middle East Technical University, Dumlupinar Blv, No:1, 06800 Cankaya, Ankara, Turkey

Brittany R. Hoard, Prof. Sang Eon Han
Department of Chemical and Nuclear Engineering, The University of New Mexico, 1 University of New Mexico, Albuquerque, NM 87131

Main text

As the cost of crystalline silicon solar cell modules has steadily declined in recent years, the proportion of the module cost attributable to silicon has remained stubbornly high, accounting for 30-40% of the total.[1,2] Promising approaches to cutting the silicon cost component of solar modules include innovative module designs with miniature concentrators;[3] cell designs that leverage lower purity, low cost silicon;[4] and utilizing new manufacturing strategies such as epitaxial silicon growth on porous silicon[5,6] or direct wafering[7] to reduce the volume of silicon used in a photovoltaic cell. The latter strategy in particular has sparked a flurry of research addressing an impediment to the realization of ultrathin crystalline silicon cells: how to maintain competitively high efficiencies while shrinking the volume of silicon available to absorb incident photons. We overcome this challenge by incorporating a unique light-trapping periodic surface nanostructure into an

ultrathin silicon film, resulting in a substantial advance in short-circuit current and efficiency over previous efforts.

As an indirect bandgap material, silicon photovoltaics are handicapped by poor absorption in the near-infrared wavelengths, which becomes particularly problematic for thin devices and can lead to unacceptable photocurrent loss. A range of strategies have been promoted to address this issue by confining electromagnetic energy in the device to increase absorption, including various nanostructured surface light trapping designs,[8-16] Bragg reflectors coupled with rear diffraction gratings,[17,18] and nanoparticles for plasmonic scattering and absorption enhancement.[19-23] Experiments have confirmed that many of these concepts increase absorption and some have been integrated into photovoltaic devices, but to date there has yet to be experimental confirmation of high photocurrent – and associated high efficiency – in a crystalline silicon device thinner than 20 μm based on an advanced light-trapping design.

In parallel, research has proceeded apace on the development of crystalline silicon photovoltaics using thin and ultrathin substrates and much less silicon than the conventional 180 μm of commercial offerings. Notable results include a 21.5% efficient, 47 μm device using a substrate thinning approach,[24] and 19.1% and 16.8% efficient cells 43- and ~20-μm-thick, respectively, using epitaxial deposition and a porous silicon transfer process.[5,25] All use conventional surface texturing approaches – randomly spaced and sized upright pyramids greater than 1 μm in height - to increase absorption. (For reference, the best reported single-junction silicon solar cell of any thickness has an efficiency of 25.6% and short-circuit current (J_{SC}) of 41.8 mA cm^{-2}.[26]) For devices as thin as 10 μm, however, fabricating efficient crystalline silicon photovoltaics with integrated nanophotonic light management structures has proven very challenging given the combined optical and electronic design demands. Successes include 10-μm-thick devices with a nanocone surface light-trapping structure and 13.7% efficiency,[27] nanowire solar cells with 5.3% efficiency,[28] and 3-μm-thick devices

2

with a nanocylinder surface texturing and 8.5% conversion efficiency.[29] In spite of these advances, the current delivered by existing devices with advanced light-trapping structures is not commensurate with the potential indicated by simulation.

The 10-μm-thick crystalline silicon photovoltaics with peak efficiency of 15.7% that we present in this article incorporate our design for a two-dimensional inverted nanopyramid surface texture and rear metallic reflector light-trapping structure that has been previously shown to possess excellent anti-reflection and long-wavelength absorption capabilities.[10,11] The device provides near-Lambertian absorption across the bulk of the spectrum from 500-1100 nm. Peak short-circuit current measures 34.5 mA cm^{-2}, marking a substantial improvement over previous devices in this thickness range. Through an analysis of current loss mechanisms, we quantify the sources of current loss in the device to focus attention on specific areas of improvement. Much of the potential for additional current gain is dependent on reducing parasitic absorption losses in the back aluminum reflector and nitride anti-reflection coating (ARC), while improvements to the device design that increase open-circuit voltage (V_{OC}) could yield device efficiencies competitive with current commercial crystalline silicon photovoltaics while requiring some 30 times less material than a standard 160 μm commercial wafer (assuming 140 μm of kerf loss).

The current and efficiency advances of our ultrathin crystalline silicon photovoltaics are rooted in optical design. The surface is patterned with a two-dimensional photonic crystal of inverted pyramids on a 700 nm pitch (**Figure 1a-1e**). In concert with the rear dielectric/aluminum reflector stack, the structure leverages wave optics effects to efficiently couple long wavelength photons into waveguide modes supported by the thin film, increasing the likelihood of absorption. Reflection from the top surface is suppressed by an index-matched (n = 1.9) 100 nm high quality PECVD silicon nitride ARC and the gently sloping 54.7° angle of the pyramids. The optical performance has been shown quantitatively to be among the best yet designed for broadband absorption in crystalline silicon.[11]

3

Exceptional absorption, in spite of such a thin absorbing layer, underpins the design's power conversion efficiency. We focus on the characteristics of two devices, the structure of which is given in Figure 1a: the one yielding the highest efficiency, Device A, and the highest short-circuit current, Device B. In both cases, for the wavelength range 400-920 nm, greater than 90% of photons are absorbed (Figure 1f). The impact of the optical design is most apparent for wavelengths longer than 800 nm, where the photonic absorption depth in silicon rapidly lengthens beyond 10 μm and the ability of a planar silicon film to absorb effectively diminishes. In comparison with a Lambertian absorber − an idealized randomizing surface that commonly serves as a theoretical benchmark for absorption in a film of a given thickness, plotted in Figure 1f for a bare silicon film with zero front surface reflection and perfect back surface reflection − the inverted nanopyramid array also performs very well. It should be noted that at longer wavelengths a portion of the measured absorption in the device takes place in the rear aluminum reflector, estimated from simulation to be approximately 1.5%, 7%, and 30% of total absorption at λ=800, 950, and 1100 nm, respectively. As a result, measured total absorption is higher than the Lambertian reference for λ>1000 nm; absorption in the silicon film − the proper comparison with a Lambertian silicon absorber − can be estimated by subtracting the aluminum component and is correctly sub-Lambertian for λ>1000 nm.

It is of paramount importance to take into account both photonic *and* electronic transport when specifying material and geometric requirements in solar cell design. These parameters constrain the design of thin crystalline silicon devices even further, and were carefully selected to maximize overall performance. For example, the PECVD silicon nitride ARC, in addition to its optical role, also affords excellent surface passivation, with measured recombination velocities on lightly-doped p-type silicon of 5-10 cm sec^{-1} (Sinton Instruments, WCT-120). An advantage of the use of potassium hydroxide (KOH) to form the surface photonic crystal is the atomically smooth surface it yields, minimizing the creation of

unnecessary excess surface area and associated recombination sites. The 250 nm rear thermal oxide is preserved over much of the back surface to reduce absorption losses in the 600 nm backside aluminum reflector,[14,27] but it also provides back surface passivation for the silicon bulk. Finally, we elect to use an aluminum mirror, which doubles as the back electrical contact through 25 μm holes etched in the oxide on a 75 μm pitch for 10% areal coverage. Although silver would provide better optical performance with lower parasitic absorption, aluminum offers a superior ohmic contact with p-type silicon while still serving as an acceptable back reflector.

The electronic design considerations, combined with excellent trans-spectral absorption, deliver high quantum conversion efficiencies. Between 440 and 850 nm, the EQE exceeds 80% (Figure 2g). For $\lambda<450$ nm and $\lambda>850$ nm, the light-trapping structure plays an important role in raising quantum efficiency, but it can be seen that the EQE still decays in both ranges. Compounding the effect of higher reflection below 450 nm, EQE is reduced by surface and Auger recombination as these high-energy photons are largely absorbed within the heavily-doped n-type emitter, ~600 nm thick. Above 850 nm, EQE begins to roll below 80% and fall rapidly after 970 nm. In addition to the negative impact of declining absorption discussed in the preceding paragraphs, a major driver of the decline in EQE is parasitic photon absorption in aluminum and nitride. Parasitic absorption is particularly strong in the back contact regions where the aluminum is not cladded by oxide. The remainder of the back aluminum reflector is also affected by parasitic absorption, although to a reduced degree since the oxide works to channel electromagnetic energy away from the rear aluminum reflector.

Elevated spectrum-wide quantum efficiency translates to high short circuit current, a key component of power conversion efficiencies greater than 15% (Figure 1h). The 34.5 mA cm^{-2} short-circuit current of Device B marks a new record for crystalline silicon devices of 10 μm thickness, only 5 mA cm^{-2} less than the 39.6 mA cm^{-2} for a 10 μm Lambertian absorber. Device A, with a slightly lower current (33.9 mA cm^{-2}) but superior fill factor sets a new

power conversion efficiency mark at 15.7%. The EQE measurements corroborate the J_{SC} data. For both devices, the open-circuit voltage is around 590 mV, allowing ample room for improvement.[27] We explore potential origins of reduced V_{OC} through simulation.

The efficiency increase is largely a result of gains in short-circuit current, while the voltage offers margin for improvement. We developed an integrated photonic/electronic transport model to guide the design and development of these nanostructured thin-film solar cells, which can also be used to gain insight into potential sources of V_{OC} degradation that adversely impact overall device efficiency. Carrier generation profiles are computed by finite element analysis, which then drive the solution to the electron flow problem applied to a two-dimensional analogue of the physical devices (**Figure 2a**). Full three-dimensional simulation is restricted by computational requirements for the electronic model.

One of the most likely culprits for the loss of voltage is the lack of a heavily-doped p^+ region in the vicinity of the rear contact holes, without which minority carriers will readily recombine at the rear contacts.[31] Figure 2b captures the voltage roll-off as the strength of the p^+-doping in the rear contact region is reduced from 5×10^{20} cm^{-3} to the level of the bulk (3×10^{16} cm^{-3}). The final step in the fabrication process is a forming-gas anneal, which augments the p-type character of the silicon contact region through aluminum diffusion. Yet it is possible the doping level is insufficient to stem back contact recombination losses. A design that included a controlled, local p^+-diffusion/implantation – typical for high-efficiency designs[32] – could yield substantial V_{OC} improvements.

A second suspect for V_{OC} degradation is surface passivation and material quality. Thin devices have the advantage of being more tolerant to lower lifetime material, but they are less resilient to high surface recombination velocities. V_{OC} generally rises logarithmically with increasing lifetime, plateauing at a value dictated by surface recombination velocity (Figure 2c). In our device design, recombination at the rear oxide/silicon interface may be higher than desired because silicon dioxide does not passivate p-type silicon particularly well.[33] The

final "alneal" – annealing aluminum on top of oxide in forming gas – improves recombination characteristics at the rear surface,[34] but more advanced rear surface passivation techniques would boost V_{OC} and efficiency, particularly given the thinness of the devices and the attendant importance of surfaces.

Although bulk lifetime is less impactful on voltage and efficiency in thin devices than thick ones, low bulk lifetime adversely affects performance, particularly for well-passivated devices (Figure 2d). It is understood that the manufacture of an SOI device layer can lead to a reduction in lifetime, a potential cause of the lower V_{OC} measured in our devices. Interestingly, as lifetime decreases, the optimal thickness of a silicon device for peak efficiency also decreases. As shown in Reference 35 – and given assumptions about surface recombination and absorption effectiveness – for bulk lifetimes below 10 µs the optimal thickness of a silicon photovoltaic is less than 20 µm. Although low bulk lifetime might contribute to the observed V_{OC} degradation, the device thinness is rather ideal for mitigating the effects of low bulk lifetime.

One standard reference sun radiates approximately 2.73 x 10^{17} photons cm^{-2} s^{-1} between 300 nm and 1105 nm, giving a maximum short circuit current of 43.7 mA cm^{-2} for a silicon solar cell with a 1.12 eV bandgap (AM1.5G spectrum). Although the 34.5 mA cm^{-2} peak J_{SC} for the devices presented here is a substantial improvement over previous results, we seek to understand the origins and magnitude of current loss to better inform strategies for improvement. Through the synthesis of empirical absorption and quantum efficiency data with results from simulation we present an analysis of the various destinies of the sum total of photons incident on device B from the sun based on the AM1.5G spectrum (**Figure 3, Table 1**). Lambertian absorption is included for reference, defined as:[36,37]

$$A = \frac{1 - e^{-4\alpha\ell}}{1 - (1 - \frac{1}{n^2})e^{-4\alpha\ell}}$$

(1)

7

where n and κ are the real and imaginary refractive indices, respectively, ℓ is the material thickness, and the attenuation coefficient $\alpha = 4\pi\kappa\lambda^{-1}$. The units of the ordinate are translated into short-circuit current per unit area and wavelength (mA cm^{-2} nm^{-1}) to connect the contribution of specific wavelength ranges to actual device current.

The most conspicuous observation from this photon flow analysis is the fall-off in absorbed and converted photons beyond 970 nm. In this range, the exponential increase in the photonic absorption length (i.e., the length required to absorb $(1-e^{-1}) = 63\%$ of incident photons, given by $(4\pi\kappa\lambda^{-1})^{-1}$) in silicon becomes problematic for ultrathin cells; whereas at λ=950 nm the absorption length is 60 μm, by λ=1000 nm it is 200 μm. The difficulty of converting these long-wavelength photons to current is illustrated by the rapid decline of the Lambertian absorber. In comparison to the Lambertian reference, however, the inverted nanopyramid structure functions extremely well. As a result of parasitic absorption in the back reflector and contacts, for λ>1000 nm total absorption actually exceeds Lambertian. The consequence is that a significant fraction of absorbed photons in the λ>970 nm regime are not converted to photocurrent. Amongst other strategies, photon conversion enhancement could be improved by reducing the size of the rear contact, where parasitic absorption is highest.

Summing the contribution of absorbed, collected, and lost current into 100 nm wide wavelength "bins" as in Table 1 allows for rapid quantitative assessment of the strengths and deficits of these devices from the perspective of current collection. For example, in the range 300≤λ<395 nm, Device B converts only 62% of incident photons to useful current after absorbing 85%, whereas an ideal Lambertian film would absorb 100% of incident photons. Absorption in this range is reduced in part by reflection losses from the nitride-coated surface, which is a direct consequence of optimizing the nitride coating and structure design for the higher photon flux regime of λ>500 nm. Reflection losses are also enhanced by the finite ridge of silicon separating one inverted nanopyramid from another that in these devices is ~75-100 nm wide; reducing this width would lead to improved absorption in the short

8

wavelength range.[11] Additionally, collection of minority carriers is relatively low for short wavelengths since carriers generated so close to the surface often recombine at the surface or through Auger recombination in the heavily-doped emitter. However, only 1.22 mA cm^{-2} worth of current density is available from the solar spectrum in this range, and even double-digit percentage gains in absorption or collection efficiency would contribute negligibly to overall short-circuit current and device efficiency.

For wavelength ranges $\lambda > 495$ nm, the cells absorb all but 1-3% of possible photons compared to a Lambertian absorber, although conversion of the generated carriers to current can still be improved upon. Photon conversion to current is very high for $495 \leq \lambda < 795$ nm, where the solar flux is at its peak. In fact, only 1.64 mA cm^{-2} of potential short-circuit current density is lost over that wavelength range. Potential improvements could be most readily sought in the $395 \leq \lambda < 495$ nm and $795 \leq \lambda < 895$ nm ranges, where collection efficiencies of 81% are found despite photon absorption rates of 94% and 96%, respectively. As mentioned earlier, losses primarily result from recombination in the emitter for the former, and parasitic photon absorption by aluminum and backside recombination for the latter.

The solar cells presented in this article realize the potential of new light-trapping designs to deliver high current and efficiencies in ultrathin crystalline silicon devices. Although the fabrication approach – using SOI wafers and IC fabrication equipment – is not commercially relevant, we succeed in demonstrating commercially-competitive performance while using more than an order of magnitude less silicon. Absorption approaches the Lambertian case over much of the relevant spectral range, and the devices convert these photons to current carriers very efficiently. From an optical perspective, advances in design that limit parasitic absorption in the rear reflector would be the most impactful. One approach could involve the inclusion of a Bragg reflector in lieu of a metal,[17] although doing so in a cost-effective manner could prove challenging. We conclude by noting that significant challenges remain in designing fabrication flows and handling procedures for thin-film

crystalline silicon solar cells, but the progress being made in that arena suggests that the promise of this light-trapping design to reduce module costs by cutting silicon material requirements is attainable.

Experimental section

Device fabrication: Devices were fabricated on 6" SOI wafers (Vendor: Ultrasil; device layer: 10 μm thick, p-type, ρ=0.6-0.85 Ω-cm; buried oxide layer: 250 nm thick; handle layer: 500 μm thick, p-type, ρ=1-5 Ω-cm) using standard semiconductor processes. Each cell was one square centimeter in area, defined precisely using lithography and electrically isolated by etching away the surrounding silicon device layer to form a mesa structure. Please see the Supplementary Information for fabrication process flow details.

Integrated optical/electronic FEA simulation: We implemented a combined optical/electronic FEA simulation using the wave optics and semiconductor modules of COMSOL Multiphysics[®]. Generation profiles of electron-hole pairs are simulated using the wave optics module and imported into the semiconductor module for electrical simulation using the drift-diffusion model. Standalone optical simulations are run in three dimensions. Optical simulation for use with the electrical model are run in two dimensions, limited by the computational requirements of the electrical model.

Top contact and bottom contact separations are set at 141.4 μm and 52.5 μm, respectively. The width of the top contact is 2.8 μm and that of the bottom contact is 21 μm, with the top contact removed for optical simulation. Total thickness (pyramid-tip to bottom) of silicon is taken as 10 μm with the 700-nm-pitch inverted pyramids etched into the silicon. 100-nm-thick silicon nitride is added on top of the textured silicon. Doping levels are set to: 2×10^{16} cm^{-3} (constant) for the p-type body, 2.5×10^{19} cm^{-3} (peak, Gaussian profile) for the implanted n$^+$ region with a junction depth of 500 nm, and 1.4×10^{20} cm^{-3} (peak, Gaussian

profile) for the implanted n^{++} region with a junction depth of 500 nm. The doping level of the p^+ region is set at 1.4×10^{20} (peak, Gaussian profile) for the simulations shown in Figure 2c and 2d but is variable in Figure 2b, with a junction depth of 500 nm. In all simulations, the bandgap is taken to be 1.12 eV at a constant temperature of 300 K. The emitter lifetime is Auger-limited.

Device characterization: The IV characteristics of the devices were measured using a Keithley 2400 sourcemeter and a 100 mW cm^{-2} solar simulator from PV Measurements with a 1300 W xenon lamp, AM1.5G filter, and a Newport Oriel 68951 flux controller calibrated by an NREL-certified Si reference cell.

Quantum efficiency was measured in 10 nm increments by first recording the photon flux from a Newport Oriel 74125 monochromator using a calibrated Newport Oriel 71675_71580 silicon photodiode connected to a power meter (Newport 2936-R). The current output from the solar cells was then measured using the monochromator at the same settings and a Keithley 2400 sourcemeter.

Absorptance was measured using a Newport Oriel 74125 monochromator, a Newport Oriel 70672 integrating sphere, and a calibrated silicon photodiode (Newport Oriel 71675_71580) connected to a Newport 2036-R power meter. Light from the monochromator entered through the topmost port of the 6-port sphere, illuminating a rectangular area approximately 1 mm x 5 mm on a sample die situated at the far port. The 1 cm^2 sample dies fit entirely within the 1-inch diameter measurement port. The samples were angled at 8° to using a custom-machined wedge, and a custom-designed port with an 8° angle and the same Spectralon® diffuse reflecting coating as the inside of the integrating sphere ensured that photons from high-order reflection modes were channeled into the sphere. The measurement was repeated using a diffuse reflective reference sample (Avian Technologies, FWS-99-02c)

to convert the measured signal strength into absolute absorptance. Measurements were corroborated with a specular reflective sample (Thorlabs, PF20-03-G01).

Supporting Information
Supporting Information is available from the Wiley Online Library or from the author.

Received: ((will be filled in by the editorial staff))
Revised: ((will be filled in by the editorial staff))
Published online: ((will be filled in by the editorial staff))

[1] D. M. Powell, M. T. Winkler, A. Goodrich, T. Buonassisi, T. *IEEE J. Photovolt*. **2013**, *3*, 662.

[2] SEMI. *International Technology Roadmap for Photovoltaic (ITRPV), 5th Ed.* < http://www.itrpv.net/.cm4all/iproc.php/Reports%20downloads/ITRPV_2014_Roadmap_ Revision1_140324.pdf?cdp=a> **2014**.

[3] J. Yoon, A. J. Baca, S.-I. Park, P. Elvikis, J. B. Geddes III, L. Li, R. H. Kim, J. Xiao, S. Wang, T.-H. Kim, M. J. Motala, B. Y. Ahn, E. B. Duoss, J. A. Lewis, R. G. Nuzzo, P. M. Ferreira, Y. Huang, A. Rockett, J. A. Rogers, *Nature Mater.* **2008**, *7*, 907.

[4] J. Y. Kwon, D. H. Lee, M. Chitambar, S. Maldonado, A. Tuteja, A. Boukai, *Nano Lett*. **2012**, *12*, 5143.

[5] J. H. Petermann, D. Zielke, J. Schmidt, F. Haase, E. G. Rojas, R. Brendel, *Prog. Photovolt.: Res. Appl*. **2011**, *20*, 1.

[6] R. Brendel, R. Auer, H. Artmann, *Prog. Photovolt.: Res. Appl*. **2001**, *9*, 217.

[7] M. LaMonica, *MIT Tech. Rev.* <http://www.technologyreview.com/featuredstory/524551/solar-survivor/> **2014**.

[8] E. R. Martins, J. Li, Y. Liu, V. Depauw, Z. Chen, J. Zhou, T. F. Krauss, *Nature Commun*. **2013**, *4*, 2665.

[9] P. Kowalczewski, M. Liscidini, L. C. Andreani, *Opt. Express* **2013**, *21*, A808.

[10] C. Schuster, A. Bozzola, L. C. Andreani, T. F. Krauss, *Opt. Express* **2014**, *22*, A542.

[11] A. Mavrokefalos, S. E. Han, S. Yerci, M. S. Branham, G. Chen, *Nano Lett*. **2012**, *12*, 2792.

[12] M. D. Kelzenberg, S. W. Boettcher, J. A. Petykiewicz, D. B. Turner-Evans, M. C. Putnam, E. L. Warren, J. M. Spurgeon, R. M. Briggs, N. S. Lewis, H. A. Atwater, *Nature Mater*. **2010**, *9*, 239.

[13] Y. M. Song, J. S. Yu, Y. T. Lee, *Opt. Lett*. **2010**, *35*, 276.

[14] S. E. Han, G. Chen, *Nano Lett*. **2010**, *10*, 4692.

[15] J. Zhu, Z. Yu, G. F. Burkhard, C.-M. Hsu, S. T. Connor, Y. Xu, Q. Wang, M. McGehee, S. Fan, Y. Cui, *Nano Lett*. **2009**, *9*, 279.

[16] M. Ernst, R. Brendel, *Phys. Status Solidi RRL* **2014**, *8*, 235.

[17] L. Zeng, P. Bermel, Y. Yi, B. A. Alamariu, K. A. Broderick, J. Liu, C. Hong, X. Duan, J. Joannopoulos, L. C. Kimerling, *Appl. Phys. Lett.* **2008**, *93*, 221105.

[18] P. Bermel, C. Luo, L. Zeng, L. C. Kimerling, J. Joannopoulos, *Opt. Express* **2007**, *15*, 16896.

[19] M. A. Green, S. Pillai, *Nature Photon.* **2012**, *6*, 130.

[20] H. A. Atwater, A. Polman, *Nature Mater.* **2010**, *9*, 205.

[21] F. J. Beck, A. Polman, K. R. Catchpole, *J. Appl. Phys*. **2009**, *105*, 114310.

[22] R. Pala, J. White, E. Barnard, J. Liu, M. Brongersma, *Adv. Mater*. **2009**, *21*, 3504.

[23] K. R. Catchpole, A. Polman, *Opt. Express* **2008**, *16*, 21793.

[24] J. Zhao, A. Wang, S. R. Wenham, M. A. Green, *Proc. 13th EU PVSEC* **1995,** 1566.

[25] L. Wang, J. Han, A. Lochtefeld, A. Gerger, M. Carroll, D. Stryker, S. Bengston, M. Curtin, H. Li, Y. Yao, D. Lin, J. Ji, A. Lennon, R. Opila, A. Barnett, *Proc. 28th EU PVSEC, 3DV.1.12.* **2013**, 2641.

[26] M. A. Green, K. Emery, Y. Hishikawa, W. Warta, E. D. Dunlop, *Prog. Photovolt.: Res. Appl*. **2014**, *22*, 701.

[27] S. Jeong, M. D. McGehee, Y. Cui, *Nature Commun*. **2013**, *4*, 2950.

[28] E. Garnett, P. Yang, *Nano Lett*. **2010**, *10*, 1082.

[29] K. J. Yu, L. Gao, J. S. Park, Y. R. Lee, C. J. Corcoran, R. G. Nuzzo, D. Chanda, J. A. Rogers, *Adv. Energy Mater*. **2013**, *3*, 1401.

[30] M. A. Green, *Sol. Energy Mater. Sol. Cells* **2008**, *92*, 1305.

[31] A. W. Blakers, A. Wang, A. M. Milne, J. Zhao, M. A. Green, *Appl. Phys. Lett.* **1989**, *55*, 1363.

[32] A. Wang, J. Zhao, M. A. Green, *Appl. Phys. Lett*. **1990**, *57*, 602.

[33] A. G. Aberle, *Prog. Photovolt.: Res. Appl.* **2000**, *8*, 473.

[34] S. Kontermann, A. Wolf, D. Reinwand, A. Grohe, D. Biro, R. Preu, *Prog. Photovolt.: Res. Appl.* **2009**, *17*, 554.

[35] A. Bozzola, P. Kowalczewski, L. C. Andreani, *J. Appl. Phys*. **2014**, *115*, 94501.

[36] E. Yablonovitch, *J. Opt. Soc. Am.* **1982**, *72*, 899.

[37] M. A. Green, *Prog. Photovolt.: Res. Appl.* **2002**, *10*, 235.

Figure captions

Figure 1. a) Optical image and schematic of a 10-μm-thick crystalline silicon photovoltaic cell with an integrated periodic surface light-trapping structure. b) SEM image of a top contact finger at the device edge highlighting the mesa isolation structure. c) SEM cross-section of the full device. d-e) High-magnification SEM images of d) a cross-section emphasizing the surface structure and nitride ARC and e) a quartet of sub-micron-scale inverted pyramids. f-h) Experimentally-measured f) absorptance, g) external quantum efficiency, and h) current density-voltage (J-V) characteristics of devices A (highest efficiency) and B (highest current) and a planar reference cell. The emprical data plotted in f) depict total absorption, which includes parasitic absorption in the aluminum and silicon nitride layers; simulated parasitic aluminum absorption is plotted using results from transfer matrix method calculations. Ideal Lambertian absorption is plotted for a 10-μm-thick silicon slab using silicon optical indices from Ref. 30.

Figure 2. a) Schematic of the structure used for integrated electrical and optical finite element simulation (not to scale). The top contact metal shown is removed during optical simulation and front surface recombination velocity is fixed at 5 cm/sec. b) Simulated V_{OC} and efficiency as a function of p^+-dopant concentration at the back contact with rear surface recombination velocity and SRH minority carrier lifetime fixed at 30 cm s^{-1} and 30 μs, respectively. The insets show how the electron concentration profile changes with rear p^+-doping at an operating voltage (V_a) = 0.56V. c-d) Simulated open-circuit voltage c) and power conversion efficiency d) as a function of bulk lifetime and back oxide surface recombination velocity ($S_{rear\ surface}$).

Figure 3. Spectral distribution of absorbed photons, collected carriers, and loss mechanisms as a function of wavelength for device B under short-circuit conditions ($V_a = 0V$). The units

of the ordinate are presented in terms of potential (or actual) short circuit current contribution per unit area per wavelength (mA cm^{-2} nm^{-1}). The area under the entire colored envelope corresponds to the total photon flux of the solar spectrum (AM1.5G), whereas that under the red envelope gives the measured output current. Total absorption, given by the area under the dashed black line, includes photons absorbed parasitically as well as in the silicon absorber. Lambertian absorption is plotted as a reference. The converted current, total absorption, and reflection are from direct measurement; loss mechanisms (aside from reflection) are inferred from simulation. See Supporting Information for details on the calculation methodology.

Tables

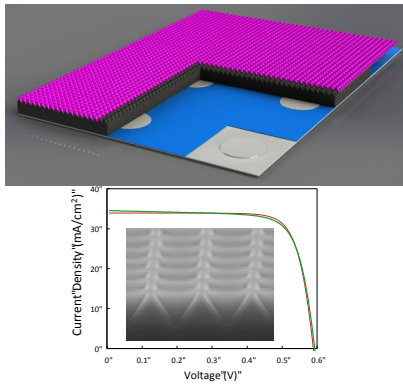**Table 1** | Tabulated photon flux analysis data in 100 nm wavelength intervals

Wavelength range (nm)	Solar flux	Photon flux/Current (mA cm^{-2})			% Solar flux		
		Lambertian limit	Total absorption	Collected	Lambertian Limit	Total absorption	Collected
$300 \leq \lambda < 395$	1.22	1.22	1.04	0.76	100%	85%	62%
$395 \leq \lambda < 495$	4.92	4.92	4.63	4.00	100%	94%	81%
$495 \leq \lambda < 595$	6.66	6.66	6.51	6.16	100%	98%	93%
$595 \leq \lambda < 695$	7.27	7.27	7.17	6.81	100%	99%	94%
$695 \leq \lambda < 795$	6.85	6.85	6.71	6.17	100%	98%	90%
$795 \leq \lambda < 895$	6.57	6.53	6.28	5.35	99%	96%	81%
$895 \leq \lambda < 995$	4.27	3.84	3.57	2.89	90%	84%	68%
$995 \leq \lambda < 1105$	5.97	2.72	3.52	1.92	46%	59%	32%

Crystalline silicon solar cells only ten micrometers thick deliver short-circuit current of 34.5 mA cm^{-2} and power conversion efficiency of 15.7%. The record performance for a crystalline silicon solar cell of such thinness is enabled by an advanced light-trapping design incorporating a 2D inverted pyramid photonic crystal and a rear dielectric/reflector stack.

M. S. Branham, W.-C. Hsu, S. Yerci, J. Loomis, S. V. Boriskina, B. R. Hoard, S. E. Han, G. Chen*

15.7% Efficient 10-μm-Thick Crystalline Silicon Solar Cells Using Periodic Nanostructures

ToC figure